Chemical Science

ROYAL SOCIETY OF CHEMISTRY

EDGE ARTICLE

View Article Online
View Journal | View Issue

Cite this: *Chem. Sci.*, 2021, **12**, 247

All publication charges for this article have been paid for by the Royal Society of Chemistry

On-surface synthesis of singly and doubly porphyrin-capped graphene nanoribbon segments†

Luis M. Mateo, ‡[ab] Qiang Sun, ‡[df] Kristjan Eimre, [d] Carlo A. Pignedoli,[d] Tomas Torres, *[abc] Roman Fasel *[de] and Giovanni Bottari *[abc]

Received 6th August 2020
Accepted 26th October 2020

DOI: 10.1039/d0sc04316h

rsc.li/chemical-science

On-surface synthesis has emerged as a powerful tool for the construction of large, planar, π-conjugated structures that are not accessible through standard solution chemistry. Among such solid-supported architectures, graphene nanoribbons (GNRs) hold a prime position for their implementation in nanoelectronics due to their manifold outstanding properties. Moreover, using appropriately designed molecular precursors, this approach allows the synthesis of functionalized GNRs, leading to nanostructured hybrids with superior physicochemical properties. Among the potential "partners" for GNRs, porphyrins (Pors) outstand due to their rich chemistry, robustness, and electronic richness, among others. However, the use of such π-conjugated macrocycles for the construction of GNR hybrids is challenging and examples are scarce. Herein, singly and doubly Por-capped GNR segments presenting a commensurate and triply-fused GNR–Por heterojunction are reported. The study of the electronic properties of such hybrid structures by high-resolution scanning tunneling microscopy, scanning tunneling spectroscopy, and DFT calculations reveals a weak hybridization of the electronic states of the GNR segment and the Por moieties despite their high degree of conjugation.

Introduction

Graphene nanoribbons (GNRs) hold a prime position for their potential application in nanoelectronics and spintronics thanks to their many intriguing and tunable physical properties, such as a small bandgap, remarkable stability, and extraordinary charge carrier mobility.[1–9] In contrast to their two-dimensional (2D) analogue graphene, GNRs exhibit a sizable band gap arising from the lateral confinement to less than 10 nm ribbon width. Intriguingly, their electronic properties depend strongly on the atomic structure of their edge topologies.[10] While GNRs with armchair edges (AGNRs) are (non-magnetic) semiconductors with a band gap that scales inversely with ribbon width,[11] GNRs with zigzag edges are magnetically non-trivial semiconductors with spin-polarized edge states that derive from flat bands near the Brillouin zone boundary.[12]

A simple and reproducible strategy to prepare 7-atom-wide AGNRs (7AGNRs) – the integer refers to the number of carbon atoms across the width of a GNR – with exact control over their molecular structure was reported in 2010.[13] This pioneering work involved the synthesis of GNRs by an Ullmann-type coupling reaction of 10,10′-dibromo-9,9′-bianthracene (DBBA) on the metal surface under ultrahigh-vacuum (UHV) conditions. Since that work, GNRs with different widths and edge structures have been fabricated using analogous strategies, characterized in detail,[8,12–17] and, in some cases, implemented into electronic devices.[5–8,16]

Besides the control of width and edge structure, novel GNR architectures containing heteroatoms,[18,19] or GNRs decorated with functional groups[20] or moieties[21] have been obtained using appropriately designed molecular precursors. This strategy is particularly appealing for the realization of GNRs with (i) tailored optical and electronic properties, (ii) magnetic properties, and (iii) other functions such as coordination of metal ions, *e.g.*, for catalytic activity.[22–25] While complex GNR-based materials have been successfully prepared by "wet" chemistry,[26,27] their subsequent transfer to atomically clean environments or their direct on-surface synthesis remains challenging.

Among the potential building blocks for the on-surface preparation of functionalized GNRs, porphyrins (Pors) and phthalocyanines (Pcs) are interesting candidates thanks to their

[a]*Departamento de Química Orgánica, Universidad Autónoma de Madrid, 28049 Madrid, Spain. E-mail: tomas.torres@uam.es; giovanni.bottari@uam.es*

[b]*IMDEA-Nanociencia, Campus de Cantoblanco, 28049 Madrid, Spain*

[c]*Institute for Advanced Research in Chemical Sciences (IAdChem), Universidad Autónoma de Madrid, 28049 Madrid, Spain*

[d]*Nanotech@surfaces Laboratory, Empa – Swiss Federal Laboratories for Materials Science and Technology, 8600 Dübendorf, Switzerland. E-mail: roman.fasel@empa.ch*

[e]*Department of Chemistry and Biochemistry, University of Bern, 3012 Bern, Switzerland*

[f]*Materials Genome Institute, Shanghai University, 200444 Shanghai, China*

† Electronic supplementary information (ESI) available: Procedures for synthesis, characterization data, and supplementary figures. See DOI: 10.1039/d0sc04316h

‡ These authors contributed equally to this work.

planar structure, molecular size, and electron richness.[28,29] Furthermore, these macrocycles exhibit high chemical versatility[30] and robustness,[31] which has made them very successful in applications such as gas sensing/catalysis,[32,33] light harvesting,[34,35] and molecular electronics.[36] Recently, the covalent fusion of a MnPc to short 7AGNRs has been reported.[37] The electronic properties of the zigzag end state (ZES) of the GNR are sensitively affected by the MnPc, meanwhile, the ZES at the other (pristine) short zigzag end of the GNR was not affected. Along the same line, a GNR–Por hybrid has been prepared by codeposition of DBBA with a tetra(bromophenyl) iron Por.[38] However, the different reactivity and number of reactive units of the two co-deposited precursors led to a lack of control over important aspects in the GNR–Por hybrid structure growth. In particular, the polydispersity, overall morphology, number of GNR "arms" fused around the Por core, and the symmetry of the resulting Por–GNR hybrid could not be controlled. Moreover, the latter study focused on the preservation of the Por's properties rather than the functionalization of GNRs. More recently, the first example of a GNR–Por hybrid consisting of a short GNR segment triply fused at each terminus by a Por has been reported by us.[39] The precise structure of this hybrid has been obtained by bond-resolved scanning tunneling microscopy (STM) and noncontact atomic force microscopy (nc-AFM), while scanning tunneling spectroscopy (STS), in combination with DFT calculations, revealed a low electronic gap of 0.4 eV.

Here, we report on the fabrication of 7AGNR segments of different lengths fused at either one or both of their termini with a Por macrocycle. The strategy involves the use of DBBA and a Por decorated with a bromo-bisanthryl moiety, where the macrocycle acts as a terminating unit towards the surface-supported polymerization reaction of DBBA thanks to the Por A_3B substitution pattern (with A = 2,6-dimethylphenyl; B = 10-bromo-bisanthryl). Moreover, the design of the Por precursor bearing a bisanthryl moiety offers an excellent geometric matching with the DBBA, leading to the selective formation of discrete hybrids with commensurate and triply-fused GNR–Por junctions. In order to elucidate the effect of the nature of the Por unit on the electronic properties of the resulting GNR–Por hybrids, both free-base and zinc Pors were used. Moreover, the latter Pors would prevent metalation of the free-base macrocycle with Au adatoms[40] and/or the dehydrogenation of the Por core.[29] The structural and electronic features of the obtained singly and doubly Por-capped GNR hybrids were investigated by high-resolution STM and STS as well as bond-resolved nc-AFM.

Results and discussion

Singly Por-capped GNR hybrids $\mathbf{1}(Zn)_n$ were fabricated in a two-step annealing process *via* on-surface reaction between DBBA and Por **3**(Zn) (Fig. 1a). Both derivatives were co-deposited in UHV conditions on Au(111) at room temperature. The sample

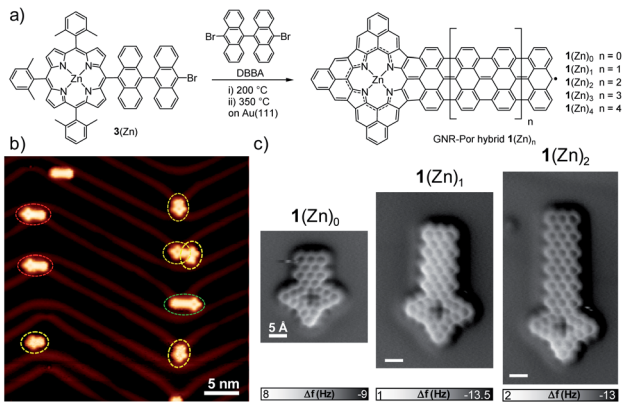

Fig. 1 (a) On-surface synthesis of singly Por-capped GNR hybrids $\mathbf{1}(Zn)_n$ from Por **3**(Zn) and DBBA. (b) STM image after the surface reaction at 350 °C on Au(111) (sample bias $V_s = -0.5$ V, tunneling current $I_t = 30$ pA) showing formation of $\mathbf{1}(Zn)_0$ (dashed yellow circle), $\mathbf{1}(Zn)_1$ (dashed red circle), and $\mathbf{1}(Zn)_2$ (dashed green circle) GNR–Por hybrids. (c) nc-AFM images of GNR–Por hybrids $\mathbf{1}(Zn)_0$, $\mathbf{1}(Zn)_1$, and $\mathbf{1}(Zn)_2$ showing the bond-resolved structures (Setpoints: −5 mV, 150–200 pA. oscillation amplitude: ∼80 pm). Scale bar: 5 Å.

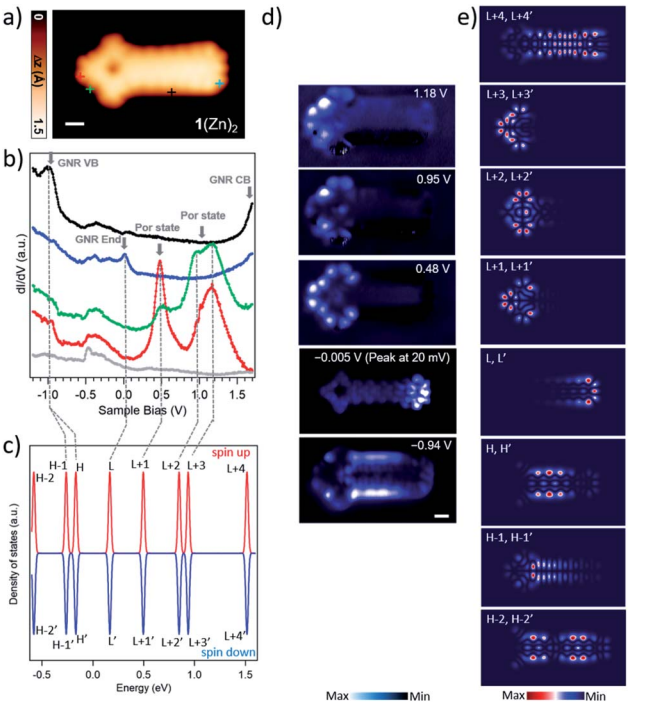

Fig. 2 (a) STM image of GNR–Por hybrid $\mathbf{1}(Zn)_2$ ($V_s = 0.48$ V, $I_t = 450$ pA) scale bar: 5 Å. (b) d*I*/d*V* spectra of $\mathbf{1}(Zn)_2$. The red, green, blue, and black d*I*/d*V* spectra were acquired over the positions indicated by markers with corresponding colors in the STM image in (a). Grey d*I*/d*V* spectra are recorded over bare Au(111). In the spectra, the arrows highlight the most prominent resonant peaks of the molecule. (c) Energy levels of the molecular orbitals of $\mathbf{1}(Zn)_2$ with two electrons being removed in gas phase, calculated by spin-polarized DFT. The energy levels are processed by Gaussian smearing to approximate the broadening of the molecular orbitals. The Fermi level is placed in the middle of the highest occupied molecular orbital (HOMO) and the lowest unoccupied molecular orbital (LUMO). The labels (L = LUMO; H = HOMO) mark the corresponding molecular orbitals, *i.e.*, L+1 represents LUMO+1. (d) Constant-current differential conductance maps recorded at the energies of the four prominent peaks, together with the constant-height current map at −0.005 V giving the spatial distribution of the LDOS for the ZES. (e) The DFT-calculated LDOS maps of $\mathbf{1}(Zn)_2$ at indicated molecular orbitals.

was then heated at ~200 °C to promote the surface-assisted Ullmann-type reaction,[41] and further heated at ~350 °C to trigger the cyclodehydrogenation reaction.[42] The formation of GNR–Por **1**(Zn)$_n$ (n = 0–2) was inferred by STM analysis (Fig. 1b and 2a) and unambiguously confirmed by bond-resolved nc-AFM microscopy (Fig. 1c). The length of the GNR segments in the hybrids was kept "short" by depositing a low coverage of DBBA and **3**(Zn) onto the surface (Fig. 1b and S2.11†). On the other hand, longer GNR–Por hybrids – up to **1**(Zn)$_9$ – could be fabricated by increasing the amount of co-deposited DBBA (Fig. 3 and S2.9†).

To gain insight into the electronic properties of GNR–Por hybrids **1**(Zn)$_n$, differential conductance dI/dV spectra were acquired on hybrids **1**(Zn)$_0$, **1**(Zn)$_1$, and **1**(Zn)$_2$ (Fig. 2 and S2.0†). On one hand, the dI/dV spectra recorded at the GNR ends of these hybrids show sharp peaks slightly above the Fermi level (blue curves in Fig. 2b and S2.0†), which stems from the positively charged ZES localized at the short zigzag edge as in the case of the previously reported 7AGNRs.[39,43,44] Evidence for the residual spin/radical localized at the GNR end of **1**(Zn)$_n$ is the observation, in some cases, of species with a doubly hydrogenated central carbon atom at the GNR terminus,[45] which suppresses the end state (Fig. 1b and S2.11†). On the other hand, dI/dV spectra acquired at positions over the Por termini of hybrids **1**(Zn)$_0$, **1**(Zn)$_1$, and **1**(Zn)$_2$ reveal striking similarities between them in terms of the position and overall shape of the resonant peaks (green and red curves in Fig. 2b and S2.0†). Additionally, differential conductance dI/dV maps of these GNR–Por hybrids exhibit analogous spatial distributions of the states at the corresponding energies (Fig. 2d and S2.0†).

Gas phase DFT calculations were carried out for **1**(Zn)$_2$ which was chosen among the three **1**(Zn)$_n$ (n = 0–2) since it provides a good "balance" between the Por character and the GNR fragment. It has been reported that π-extended Pors, Por–7AGNR hybrids, and the 7AGNR end states tend to be positively charged by the Au(111) surface.[39,43,44,46] To estimate the effect of possible interactions between the molecule and the underlying substrate, the neutral, monocationic, and dicationic GNR–Por **1**(Zn)$_2$ hybrids were simulated. For the dicationic species, an excellent matching between the simulated LDOS maps and the experimental dI/dV maps was found (Fig. 2c and e). This finding indicates the injection of two electrons from the hybrid to the surface.

Comparison of dI/dV mapping and DFT calculations allows to draw several conclusions. Firstly, it shows that the prominent resonances in the dI/dV spectra at around 0.48 V and 0.95 V are entirely localized on the Por units, and corresponds to the LUMO+1 and LUMO+2 of the dicationic **1**(Zn)$_2$. Secondly, it indicates that, despite the "fused" nature of the GNR–Por hybrids, the frontier states of the Por unit and the GNR end state remain rather localized and thus only weakly hybridized. In fact, the only state found to be delocalized over both the Por and GNR units is the state at −0.94 V, which comprises the contributions from the HOMO derived from the valence band (VB) of the GNR and HOMO-1 derived from the hybridization between GNR and Por (see dI/dV and simulated LDOS maps in Fig. 2c and e). Note that similar low hybridization was reported in a previous work where porphine macrocycles were unselectively fused to graphene flakes.[47] Thirdly, a state slight above the Fermi level (the peak at 20 mV) is spatially localized at the GNR zigzag end, corresponding to the LUMO of the dicationic molecule.

Besides the electronic states at the Por termini of the GNR–Por hybrids, the electronic gap of the bulk GNR segment was also investigated. For this purpose, longer GNR–Por hybrids (*i.e.*, **1**(Zn)$_3$, **1**(Zn)$_4$, and **1**(Zn)$_9$) were fabricated by increasing the amount of DBBA co-deposited (Fig. 3 and S2.9†). dI/dV spectra acquired in the central region of the GNR segment of GNR–Por hybrids **1**(Zn)$_n$ (n = 0–4 and 9) are reported in Fig. 3.

With increasing GNR segment length, the valence band maximum (VBM) – as determined from the half-maximum position of the raising slope[48] – is observed to shift from about −1.05 V for the shortest **1**(Zn)$_0$ to successively higher energies, reaching −0.75 V for **1**(Zn)$_9$. It is thus expected that the VBM of GNR–Por hybrids longer than **1**(Zn)$_9$ will converge around −0.7 V as is observed for long pristine 7AGNRs on Au(111).[48] The conduction band minimum (CBM) is more difficult to determine accurately, because spectra were unfortunately acquired only up to 1.6 eV, such that only the onset of a peak can be discerned. Nevertheless, a clear shift of this onset toward the lower bias voltage can be recognized with increasing GNR segment length. The electronic gap of the GNR segments thus shows the expected length dependence, *i.e.* a reduction of electronic gap with segment length as observed in uncapped finite-length GNRs.[49] Interestingly, closer inspection of the energy position of the Por derived frontier states reveals energy shifts with increasing GNR segment length that are very similar to the ones of the GNR segment CBM, but in opposite direction (namely toward higher energy, like the GNR segment VBM). From **1**(Zn)$_0$ to **1**(Zn)$_2$, the Por HOMO and LUMO derived resonances shift from 0.38 eV to 0.48 eV and from 0.85 eV to 0.95 eV, respectively (Fig. S2.0†). Overall, our spectroscopic data

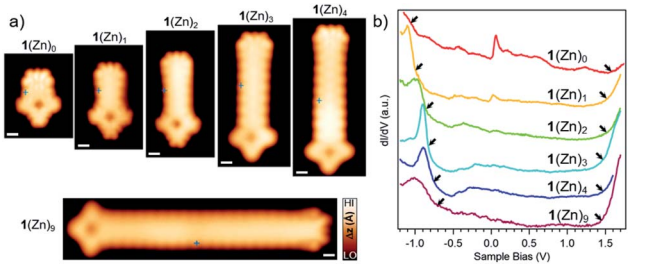

Fig. 3 (a) Close-up STM images of GNR-Por hybrids **1**(Zn)$_0$–**1**(Zn)$_4$ (from left to right: V_s = −0.1 V, I_t = 230 pA; V_s = 0.45 V, I_t = 480 pA; V_s = 0.48 V, I_t = 450 pA; V_s = −0.2 V, I_t = 150 pA; V_s = −0.2 V, I_t = 250 pA) and **1**(Zn)$_9$ (V_s = −0.06 V, I_t = 200 pA). For overview STM image for **1**(Zn)$_9$ see Fig. S2.9.† Scale bar: 5 Å. (b) dI/dV spectra recorded at the central region of the GNR segment in hybrids **1**(Zn)$_0$–**1**(Zn)$_4$ and **1**(Zn)$_9$ (spectra acquisition positions marked in the STM images in a). For each spectrum, the left arrows indicate the position of the valence band maximum as determined from the half-maximum position in the raising slope of the corresponding peak, the right arrows indicate the onset of the CBM as determined by the intersection of the linear slope with the baseline.

for $\mathbf{1}(Zn)_n$ reveal frontier orbitals originating from Por located well within the electronic band gap of the GNR segment.

Taking into account that in $\mathbf{1}(Zn)_n$ the electronic properties of the GNR segment are only marginally affected by the fused single Por end-capping, the question arises whether the same holds for doubly Por-capped GNRs. To address this question, the formation of doubly ZnPor-capped GNRs was attempted by increasing the amount of Por **3**(Zn) with respect to DBBA. However, surprisingly, this strategy was unsuccessful, as only a few homocoupled $\mathbf{2}(Zn)_0$ species were obtained along with some singly-capped short GNR fragments (predominantly $\mathbf{1}(Zn)_0$).

On the other hand, the same strategy using Por $\mathbf{3}(H_2)$ led to the successful formation of doubly Por-capped GNR hybrids $\mathbf{2}(H_2)_1$ and $\mathbf{2}(H_2)_2$ (involving the formation of 27 and 31 new C–C bonds, respectively) as well as homocoupling product $\mathbf{2}(H_2)_0$ and not coupled yet cyclodehydrogenated $\mathbf{1}(H_2)_0$ species (Fig. 4b–d) (*vide infra*).[39] To shed some light on the unexpectedly different coupling behavior of $\mathbf{3}(H_2)$ and **3**(Zn) with DBBA, a control experiment was carried out, namely, the homocoupling of the two Pors to give $\mathbf{2}(H_2)_0$ and $\mathbf{2}(Zn)_0$, respectively. As can be seen from the corresponding overview STM images, the homocoupling "yield" is strikingly lower for the Zn(II)-derivative **3**(Zn) than for its free-base analogue $\mathbf{3}(H_2)$ (Fig. S2.1†). We suspect that the incorporation of Zn(II) into the macrocycle leads to changes in its geometry upon surface absorption, which sensitively hampers the Ullmann coupling reaction, thus making a "double" coupling of the GNR with this Por highly unlikely.[50]

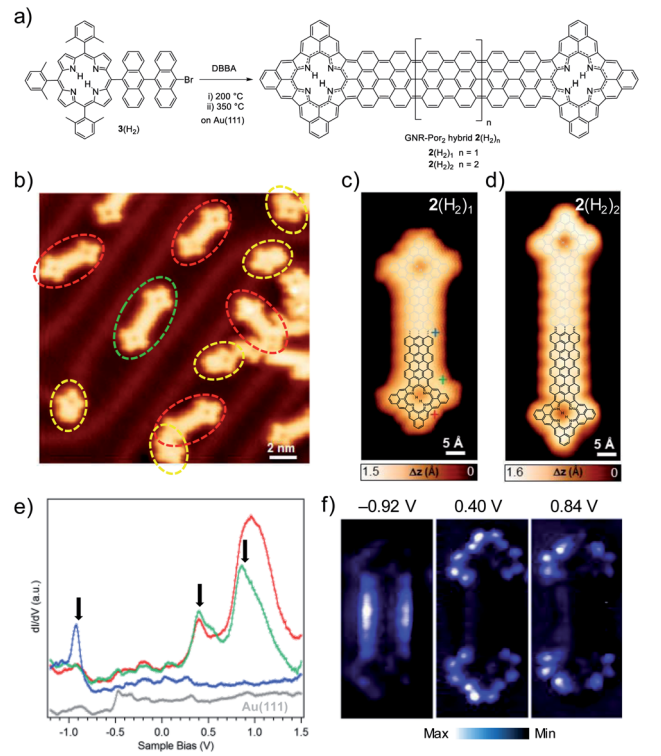

Fig. 4 (a) On-surface synthesis of doubly Por-capped GNR hybrids $\mathbf{2}(H_2)_n$ from Por $\mathbf{3}(H_2)$ and DBBA. (b) STM image after the surface reaction at 350 °C on Au(111) (V_s = 0.45 V, I_t = 80 pA) showing formation of doubly Por-capped GNR $\mathbf{2}(H_2)_0$ (dashed red circle) and $\mathbf{2}(H_2)_1$ (dashed green circle), and singly Por-capped GNR $\mathbf{1}(H_2)_0$ (dashed yellow circle). Close-up STM images of GNR–Por_2 hybrids (c) $\mathbf{2}(H_2)_1$ (V_s = 0.46 V, I_t = 100 pA) and (d) $\mathbf{2}(H_2)_2$ (V_s = −0.05 V, I_t = 200 pA) (for the overview STM image of $\mathbf{2}(H_2)_2$, see Fig. S2.10†). For a better visualization, the chemical structures of $\mathbf{2}(H_2)_1$ and $\mathbf{2}(H_2)_2$ are superimposed to the corresponding STM images. (e) Differential conductance d*I*/d*V* spectra of GNR–Por_2 $\mathbf{2}(H_2)_1$ taken at the positions indicated by markers with corresponding colors in (c). Arrows indicate the three most prominent peaks. Grey d*I*/d*V* spectrum recorded over Au(111). (f) Constant-current d*I*/d*V* maps recorded at the energies indicated by arrows in (e).

However, as seen from the STM and STS analysis of $\mathbf{2}(Zn)_0$, the metalation of the macrocycle with Zn(II) does not influence the electronic properties of this doubly Por-capped GNR hybrid compared to its free-base H_2Por analogue $\mathbf{2}(H_2)_0$ (see Fig. S2.2–S2.4†).[39] Therefore, and due to the low reactivity of Por **3**(Zn), the synthesis of longer GNR-Por_2 hybrids was carried out by co-depositing DBBA with Por $\mathbf{3}(H_2)$ instead of **3**(Zn) (Fig. 4a). Considering the possible inclusion of gold adatoms in free-base Pors – reflected by an increased apparent height in the cavity of the Pors[40] – only GNR–Por_2 hybrids containing non-metalated Pors were investigated thereafter.

Differential conductance (d*I*/d*V*) spectroscopy was used to access the electronic properties of the elongated GNR–Por_2 hybrid $\mathbf{2}(H_2)_1$. Point spectra acquired at different positions over the molecule reveal several resonances that derive from the molecular frontier orbitals around the Fermi level (highlighted by arrows in Fig. 4e). Both the energy position and the overall shape of the peaks in $\mathbf{2}(H_2)_1$ are very similar to those of $\mathbf{2}(H_2)_0$.[39] Spatially resolved d*I*/d*V* mapping at the corresponding energies shows that the occupied state at −0.92 V is mainly located on the 7AGNR segment, whereas the unoccupied states at 0.40 and 0.84 V are localized on the Por moieties (Fig. 4f). Therefore, both the STS spectroscopy and the d*I*/d*V* mapping of $\mathbf{2}(H_2)_1$ show important similarities with homocoupled $\mathbf{2}(H_2)_0$.[39] In line with the assignment of the molecular orbitals of $\mathbf{2}(H_2)_0$,[39] in $\mathbf{2}(H_2)_1$ the state at 0.40 V can be assigned to derive from the (gas phase) HOMO of the neutral hybrid, and the one at 0.84 V from the LUMO. With the gas phase HOMO fully emptied upon adsorption, the electronic structure of $\mathbf{2}(H_2)_n$ hybrids on Au(111) thus resembles the disjoint one of a donor–acceptor structure, with the highest occupied state localized on the GNR segment and the lowest unoccupied state localized on the terminal Por units, defining a gap of 1.3 eV for $\mathbf{2}(H_2)_1$ on Au(111).

Conclusions

In summary, we have reported a strategy to fabricate "elongated" singly and doubly Por-capped GNR hybrids with a commensurate and triply-fused GNR–Por junction, which was unambiguously confirmed by bond-resolved nc-AFM imaging. The study of the electronic properties of such hybrids by high-resolution STM and STS shows a weak hybridization of the electronic states of the GNR and the Por moieties despite their high degree of conjugation. Moreover, in the singly-capped GNRs, the ZES exhibits similar electronic properties as the pristine GNR even for the shortest hybrid. This work opens new

pathways towards the preparation of more sophisticated GNR–Por architectures, *e.g.* by introducing magnetic metal ions (*i.e.*, Cu, Co, Fe, *etc.*) in the macrocycle cavity to create transition metal/Por/GNR hybrid nanostructures. Such studies are currently being conducted in our laboratories.

Conflicts of interest

The authors declare no competing financial interest.

Acknowledgements

Financial support from Spanish MICINN (CTQ2017-85393-P) is acknowledged. IMDEA Nanociencia acknowledges support from the "Severo Ochoa" Programme for Centres of Excellence in R&D (MINECO, Grant SEV2016-0686). This work was supported by the Swiss National Science Foundation (200020_182015, IZLCZ2_170184) and the NCCR MARVEL funded by the Swiss National Science Foundation (51NF40-182892). Computational support from the Swiss Supercomputing Center (CSCS) under project ID s904 is gratefully acknowledged.

References

1 V. Barone, O. Hod and G. Scuseria, *Nano Lett.*, 2006, **6**, 2748–2754.
2 Z. Chen, Y.-M. Lin, M. J. Rooks and P. Avouris, *Phys. E*, 2007, **40**, 228–232.
3 X. Li, X. Wang, L. Zhang, S. Lee and H. Dai, *Science*, 2008, **319**, 1229–1232.
4 M. Koch, F. Ample, C. Joachim and L. Grill, *Nat. Nanotechnol.*, 2012, **7**, 713–717.
5 M. El Abbassi, M. L. Perrin, G. B. Barin, S. Sangtarash, J. Overbeck, O. Braun, C. J. Lambert, Q. Sun, T. Prechtl, A. Narita, K. Müllen, P. Ruffieux, H. Sadeghi, R. Fasel and M. Calame, *ACS Nano*, 2020, **14**, 5754–5762.
6 G. Borin Barin, A. Fairbrother, L. Rotach, M. Bayle, M. Paillet, L. Liang, V. Meunier, R. Hauert, T. Dumslaff, A. Narita, K. Müllen, H. Sahabudeen, R. Berger, X. Feng, R. Fasel and P. Ruffieux, *ACS Appl. Nano Mater.*, 2019, **2**, 2184–2192.
7 Z. Chen, W. Zhang, C.-A. Palma, A. Lodi Rizzini, B. Liu, A. Abbas, N. Richter, L. Martini, X.-Y. Wang, N. Cavani, H. Lu, N. Mishra, C. Coletti, R. Berger, F. Klappenberger, M. Kläui, A. Candini, M. Affronte, C. Zhou, V. De Renzi, U. del Pennino, J. V. Barth, H. J. Räder, A. Narita, X. Feng and K. Müllen, *J. Am. Chem. Soc.*, 2016, **138**, 15488–15496.
8 J. P. Llinas, A. Fairbrother, G. Borin Barin, W. Shi, K. Lee, S. Wu, B. Yong Choi, R. Braganza, J. Lear, N. Kau, W. Choi, C. Chen, Z. Pedramrazi, T. Dumslaff, A. Narita, X. Feng, K. Müllen, F. Fischer, A. Zettl, P. Ruffieux, E. Yablonovitch, M. Crommie, R. Fasel and J. Bokor, *Nat. Commun.*, 2017, **8**, 633.
9 Y.-W. Son, M. L. Cohen and S. G. Louie, *Nature*, 2006, **444**, 347–349.
10 L. Talirz, P. Ruffieux and R. Fasel, *Adv. Mater.*, 2016, **28**, 6222–6231.
11 N. Merino-Díez, A. Garcia-Lekue, E. Carbonell-Sanromà, J. Li, M. Corso, L. Colazzo, F. Sedona, D. Sánchez-Portal, J. I. Pascual and D. G. de Oteyza, *ACS Nano*, 2017, **11**, 11661–11668.
12 P. Ruffieux, S. Wang, B. Yang, C. Sanchez-Sanchez, J. Liu, T. Dienel, L. Talirz, P. Shinde, C. A. Pignedoli, D. Passerone, T. Dumslaff, X. Feng, K. Mullen and R. Fasel, *Nature*, 2016, **531**, 489–492.
13 J. Cai, P. Ruffieux, R. Jaafar, M. Bieri, T. Braun, S. Blankenburg, M. Muoth, A. P. Seitsonen, M. Saleh, X. Feng, K. Müllen and R. Fasel, *Nature*, 2010, **466**, 470.
14 Y. C. Chen, D. G. de Oteyza, Z. Pedramrazi, C. Chen, F. R. Fischer and M. F. Crommie, *ACS Nano*, 2013, **7**, 6123–6128.
15 H. Zhang, H. Lin, K. Sun, L. Chen, Y. Zagranyarski, N. Aghdassi, S. Duhm, Q. Li, D. Zhong, Y. Li, K. Müllen, H. Fuchs and L. Chi, *J. Am. Chem. Soc.*, 2015, **137**, 4022–4025.
16 L. Martini, Z. Chen, N. Mishra, G. B. Barin, P. Fantuzzi, P. Ruffieux, R. Fasel, X. Feng, A. Narita, C. Coletti, K. Müllen and A. Candini, *Carbon*, 2019, **146**, 36–43.
17 J. Cai, C. A. Pignedoli, L. Talirz, P. Ruffieux, H. Söde, L. Liang, V. Meunier, R. Berger, R. Li, X. Feng, K. Müllen and R. Fasel, *Nat. Nanotechnol.*, 2014, **9**, 896.
18 X. Y. Wang, J. I. Urgel, G. B. Barin, K. Eimre, M. Di Giovannantonio, A. Milani, M. Tommasini, C. A. Pignedoli, P. Ruffieux, X. Feng, R. Fasel, K. Mullen and A. Narita, *J. Am. Chem. Soc.*, 2018, **140**, 9104–9107.
19 S. Kawai, S. Saito, S. Osumi, S. Yamaguchi, A. S. Foster, P. Spijker and E. Meyer, *Nat. Commun.*, 2015, **6**, 8098.
20 E. Carbonell-Sanromà, J. Hieulle, M. Vilas-Varela, P. Brandimarte, M. Iraola, A. Barragán, J. Li, M. Abadia, M. Corso, D. Sánchez-Portal, D. Peña and J. I. Pascual, *ACS Nano*, 2017, **11**, 7355–7361.
21 C. Ma, Z. Xiao, A. A. Puretzky, H. Wang, A. Mohsin, J. Huang, L. Liang, Y. Luo, B. J. Lawrie, G. Gu, W. Lu, K. Hong, J. Bernholc and A.-P. Li, *ACS Nano*, 2020, **14**, 5090–5098.
22 A. Keerthi, B. Radha, D. Rizzo, H. Lu, V. Diez Cabanes, I. C.-Y. Hou, D. Beljonne, J. Cornil, C. Casiraghi, M. Baumgarten, K. Müllen and A. Narita, *J. Am. Chem. Soc.*, 2017, **139**, 16454–16457.
23 C. Rogers, W. S. Perkins, G. Veber, T. E. Williams, R. R. Cloke and F. R. Fischer, *J. Am. Chem. Soc.*, 2017, **139**, 4052–4061.
24 A. Narita, Z. Chen, Q. Chen and K. Mullen, *Chem. Sci.*, 2019, **10**, 964–975.
25 Y. Huang, Y. Mai, U. Beser, J. Teyssandier, G. Velpula, H. van Gorp, L. A. Straasø, M. R. Hansen, D. Rizzo, C. Casiraghi, R. Yang, G. Zhang, D. Wu, F. Zhang, D. Yan, S. De Feyter, K. Müllen and X. Feng, *J. Am. Chem. Soc.*, 2016, **138**, 10136–10139.
26 S. Mikhail and S. Alexander, *Phys. Sci. Rev.*, 2017, **2**, 20160108.
27 A. Narita, Z. Chen, Q. Chen and K. Müllen, *Chem. Sci.*, 2019, **10**, 964–975.
28 S. Hiroto, Y. Miyake and H. Shinokubo, *Chem. Rev.*, 2017, **117**, 2910–3043.
29 J. M. Gottfried, *Surf. Sci. Rep.*, 2015, **70**, 259–379.
30 J. S. Lindsey, *Acc. Chem. Res.*, 2010, **43**, 300–311.

31 Z. Liu, A. A. Yasseri, J. S. Lindsey and D. F. Bocian, *Science*, 2003, **302**, 1543–1545.
32 K. Seufert, M.-L. Bocquet, W. Auwärter, A. Weber-Bargioni, J. Reichert, N. Lorente and J. V. Barth, *Nat. Chem.*, 2011, **3**, 114–119.
33 Q. Chen, L. Brambilla, L. Daukiya, K. S. Mali, S. De Feyter, M. Tommasini, K. Müllen and A. Narita, *Angew. Chem., Int. Ed.*, 2018, **57**, 11233–11237.
34 M. Urbani, M. Grätzel, M. K. Nazeeruddin and T. Torres, *Chem. Rev.*, 2014, **114**, 12330–12396.
35 S. Mathew, A. Yella, P. Gao, R. Humphry-Baker, B. F. E. Curchod, N. Ashari-Astani, I. Tavernelli, U. Rothlisberger, M. K. Nazeeruddin and M. Grätzel, *Nat. Chem.*, 2014, **6**, 242–247.
36 W. Auwärter, K. Seufert, F. Bischoff, D. Ecija, S. Vijayaraghavan, S. Joshi, F. Klappenberger, N. Samudrala and J. V. Barth, *Nat. Nanotechnol.*, 2012, **7**, 41–46.
37 X. Su, Z. Xue, G. Li and P. Yu, *Nano Lett.*, 2018, **18**, 5744–5751.
38 J. Li, N. Merino-Díez, E. Carbonell-Sanromà, M. Vilas-Varela, D. G. de Oteyza, D. Peña, M. Corso and J. I. Pascual, *Sci. Adv.*, 2018, **4**, eaaq0582.
39 L. M. Mateo, Q. Sun, S.-X. Liu, J. J. Bergkamp, K. Eimre, C. A. Pignedoli, P. Ruffieux, S. Decurtins, G. Bottari, R. Fasel and T. Torres, *Angew. Chem., Int. Ed.*, 2020, **59**, 1334–1339.
40 B. Cirera, B. de la Torre, D. Moreno, M. Ondráček, R. Zbořil, R. Miranda, P. Jelínek and D. Écija, *Chem. Mater.*, 2019, **31**, 3248–3256.
41 M. Lackinger, *Chem. Commun.*, 2017, **53**, 7872–7885.
42 M. Treier, C. A. Pignedoli, T. Laino, R. Rieger, K. Müllen, D. Passerone and R. Fasel, *Nat. Chem.*, 2010, **3**, 61.
43 J. van der Lit, M. P. Boneschanscher, D. Vanmaekelbergh, M. Ijäs, A. Uppstu, M. Ervasti, A. Harju, P. Liljeroth and I. Swart, *Nat. Commun.*, 2013, **4**, 2023.
44 M. Ijäs, M. Ervasti, A. Uppstu, P. Liljeroth, J. van der Lit, I. Swart and A. Harju, *Phys. Rev. B: Condens. Matter Mater. Phys.*, 2013, **88**, 075429.
45 L. Talirz, H. Söde, J. Cai, P. Ruffieux, S. Blankenburg, R. Jafaar, R. Berger, X. Feng, K. Müllen, D. Passerone, R. Fasel and C. A. Pignedoli, *J. Am. Chem. Soc.*, 2013, **135**, 2060–2063.
46 Q. Sun, L. M. Mateo, R. Robles, P. Ruffieux, N. Lorente, G. Bottari, T. Torres and R. Fasel, *J. Am. Chem. Soc.*, 2020, **142**, 18109–18117.
47 Y. He, M. Garnica, F. Bischoff, J. Ducke, M.-L. Bocquet, M. Batzill, W. Auwärter and J. V. Barth, *Nat. Chem.*, 2016, **9**, 33.
48 P. Ruffieux, J. Cai, N. C. Plumb, L. Patthey, D. Prezzi, A. Ferretti, E. Molinari, X. Feng, K. Müllen, C. A. Pignedoli and R. Fasel, *ACS Nano*, 2012, **6**, 6930–6935.
49 L. Talirz, H. Söde, S. Kawai, P. Ruffieux, E. Meyer, X. Feng, K. Müllen, R. Fasel, C. A. Pignedoli and D. Passerone, *ChemPhysChem*, 2019, **20**, 2348–2353.
50 P. H. Jacobse, A. van den Hoogenband, M.-E. Moret, R. J. M. Klein Gebbink and I. Swart, *Angew. Chem., Int. Ed.*, 2016, **55**, 13052–13055.